Formulation of Spectral Stiffness Microplane Model for Uni-Directional Composite

Sung Lin Jason Tien

A thesis

submitted in partial fulfillment of the

requirements for the degree of

Master of Science in Aeronautics & Astronautics

University of Washington

2017

Committee:

Prof. Marco Salviato, Chair

Prof. Jinkyu Yang

Program Authorized to Offer Degree:

Aeronautics and Astronautics

University of Washington

Abstract

Formulation of Spectral Stiffness Microplane Model for Uni-Directional Composite

Sung Lin Jason Tien

Chair of the Supervisory Committee:
Assistant Professor - Marco Salviato
Department of Aeronautics and Astronautics

This thesis presents a general constitutive model to simulate the orthotropic stiffness, pre-peak nonlinearity, failure envelopes, and the post-peak softening and fracture behaviors of uni-directional composites. The framework of the microplane model is adopted and the constitutive laws are formulated in terms of stress and strain vectors acting on microplanes with different orientation. The model exploits the spectral decomposition of the transversely isotropic stiffness matrix to define orthogonal strain modes at the microplane level. A variational approach is applied to relate the microplane stresses to the continuum tensor at the macroscopic sacle. Following the formulation, a generic 2mm cube is used to perform calibration and validation to confirm with the experimental results.

TABLE OF CONTENTS

Chapter 1 7

Introduction 7

Chapter 2 11

Microplane Subroutine 11

2.1 Background of Microplane Model 11

2.2 Microplane Framework 11

2.3 Benefits of Microplane 14

Chapter 3 16

Microplane Model with Spectral Decomposition Theorem 16

3.1 Spectral Decomposition of the Elastic Tensor 16

3.2 Decomposition for Uni-directional Composite 18

3.3 Microplane Eigenstrain Distribution 21

Chapter 4 26

Material calibration and validation 26

4.1 Uniaxial Stress Strain Curves of Uni-directional Laminates 27

4.2 Calibration and Validation: Shear Mode 28

4.3 Calibration and Validation: Matrix Mode 31

4.4 Calibration and Validation: Fiber Mode 36

Chapter 5 42

Conclusion 42

5.1 Future Work 42

References 44

ACKNOWLEDGEMENTS

The author wishes to express the most sincere appreciation to the University of Washington, where he has the opportunity to work with Prof. Marco Salviato and Ph.D. student Sean Phenisee who helped the success of this research.

Chapter 1

Introduction

In the recent decades, the world has seen heavy adoptions and shifts to designing using composite materials, the most noticeable industry is undoubtedly aerospace, not only in the commercial aircraft and military planes, but also in space vehicles like satellites due to composite's strong, light weight and thermal stability characteristics. We also see an increase use of composites in other industries such as the wind energy production field where wind turbine blades have to be designed to have high resistance against fatigue, the automotive industry where the structure needs to be both light and strong to absorb energy upon impact and various civil engineering applications like bridges and construction reinforcements, just to name a few.

Composite materials draw so much attention to the engineers because of its lightweight characteristic and its high strength. Carbon fiber reinforced composite is about 70% lighter than steel and about 40% lighter than aluminum, that is why composites are especially important for industries like transportation and aeronautics, where weight plays a crucial role. In addition, composite's fatigue resistance is higher than that of traditional metals, allowing them to withstand repeated loads. It is more chemically stable with high resistance to UV damage, thermal expansion and corrosion because the use of plastic in the material configurations. One feature, however, that stands out in particular to design engineers, is that composite material has the ability to be tailored to a specific strength for their intended applications. With different resins, different reinforcements like carbon fibers or glass fibers, and the specific fiber orientations, engineers are able to customize the formulation of the composites to achieve different material properties.

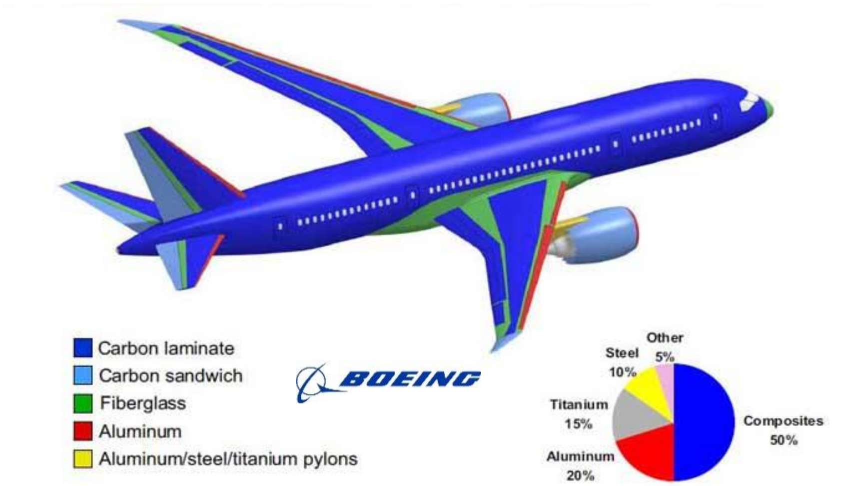

Figure 1.1: Material composition of Boeing 787 Dreamliner (Courtesy to the Boeing Company)

The best and the most representative example of composite application is of course the Boeing 787 Dreamliner, shown in Fig. 1.1. Boeing makes great use of carbon fiber reinforced plastic and other composites in its 787 airframe. In fact, 50% by weight of the entire plane is made out of different kinds of composites. This approach offers about 20% in weight savings compared to more conventional aluminum designs. This weight reduction increases the performance of the aircraft by saving fuels while maintaining its capacity of payloads. In addition, the use of composites instead of aluminum in its fuselage structure enables an increase in cabin pressure and humidity level, therefore the passengers can enjoy a more comfortable flight. On the design and analysis perspective, taking the advantage of composite's high yield stress and strength in the fiber direction, replacing aluminum in the highly tensile-loaded areas can significantly reduce the overall weight of the airframe. Further, it decreases the number of scheduled and nonroutine maintenance thanks to the composite's excellent resistance against fatigue and corrosion in comparison to aluminum structures.

As the market size of composite material keeps on growing, the outlook for composites is very promising, there can be a place for composites in every industry. According to Composites

Forecasts & Consulting (Fig. 1.2), the worldwide demand for composite material is projected to double in the next ten years or so, majority of this demand will go toward the aerospace/defense industry, as well as automotive and many other recreational fields. Therefore having a good model analyzing failure behaviors is more important than ever. It is worth mentioning that similar effort has been done for textile composites material [1]. The objective of the microplane model and the current study is to come up with a reliable model for uni-directional laminates that is both easy to calibrate for different material setups and that does not require extensive experimental data so that the end users can get accurate results fast.

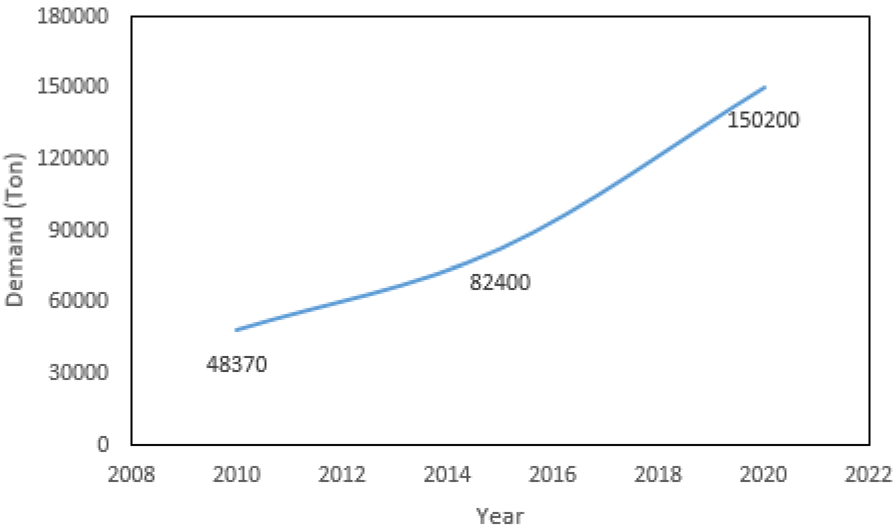

Figure 1.2: Projected worldwide demand for carbon fiber composites

Speaking of analysis, there are plenty of different algorithms and formulations available today that can analyze composites. Just to name a few famous ones: Tsai-Hill failure criterion, derived from Von Mises theorem based on isotropic material; Tsai-Wu, based on empirical data; maximum stress and maximum strain theorem, a simple check on the principle stress or strain, and lastly the Angle Minus Load theory, which is developed by Boeing and also based on a large pool of experimental data. These developed formulations and many other theories often rely solely on derivation from other theories or on empirical data so they are not capable of capturing progressive damage in the material, a feature that plays the key differentiator between simulation and real life.

For example, let us take a closer look at the Angle Minus Load (AML) theory, which is currently being implemented in the aerospace industry like Blue Origin. The theory is based on empirical data so the theory is unable to capture progressive damage or predict failure. It provides no information about the modes of failure, such as fiber failure in tension, fiber kinking or matrix cracking. It is also not capable of analyzing multi-axial loading and completely ignores the size effects [2], which is crucially importantly for design because of the fracture energy analysis. Without the capability to predict the fracture energy is the reason why the margin of safety is usually very high for composite structures. If explained schematically, the stress strain curve for a simple tension test in the fiber direction for a uni-directional lamina is illustrated in Fig. 1.3. We can see that immediately after reaching the yield stress the criterion stops working as it is not capable to predict the softening behavior of fibers whereas the Microplane model can capture the effect of progressive energy dissipation. We can clearly see that the area under the two curves, or the fracture energy needed to cause the failure of the fiber, is very different as the AML method significantly under-predict this energy.

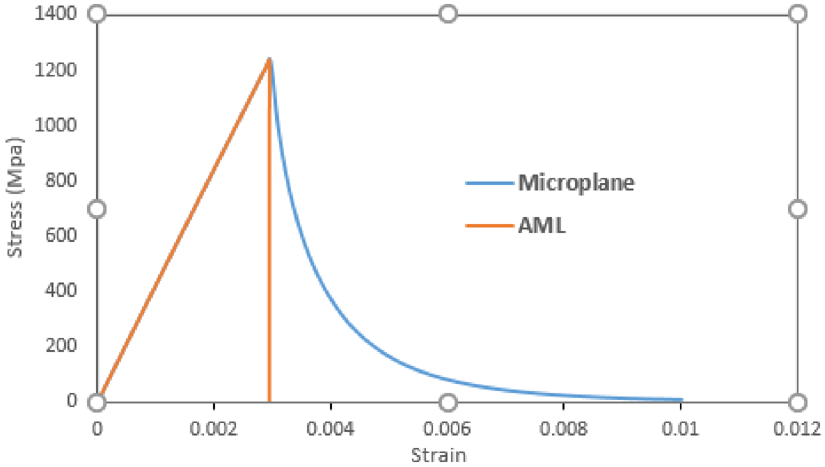

Figure 1.3: Stress-strain curve of uniaxial tension test for uni-directional composites using micoaplane subroutine and the Angle Minus Load (AML) theory

Chapter 2

Microplane Subroutine

2.1 BACKGROUND OF MICROPLANE MODEL

Inspired by the slip theory of plasticity (pioneered by Taylor [3] and formulated in detail by Batdorf and Budiansky [4]), Bazant and Oh [5] introduced the microplane model to simulate statistically isotropic materials such as concrete, exhibiting softening damage. The model captures the fact that almost all of the inelastic phenomena in the concrete microstructure, including cracking opening, frictional slip, compressive splitting and fiber pullout whereas the classical tensorial constitutive models exemplified by the theories of plasticity cannot capture these behaviors.

Since the introduction in the early 1980s, the microplane model for isotropic materials has evolved through seven progressively improved versions labeled as M1 [5],[6], M2 [7], M3 [8], M4 [9][9], M5 [11], M6 [12], M7 [13]. The microplane model has also been developed for other more complex materials such as jointed rock [14], and, clay, rigid foam, shape memory alloys, and textile composites [1].

2.2 MICROPLANE FRAMEWORK

A key feature of the microplane model is that the constitutive equations are formulated in terms of the stress and strain vectors acting on a generic plane of any orientation within the material mesostructured, called the microplane. For the element under analysis, it is covered by one eighth of a spherical volume, for which a simple schematic and its associated coordinates can be seen in

Fig. 2.1a. The microplanes can be conceived as the tangent planes of a unit sphere surrounding every point in the three-dimensional space Fig. 2.1b

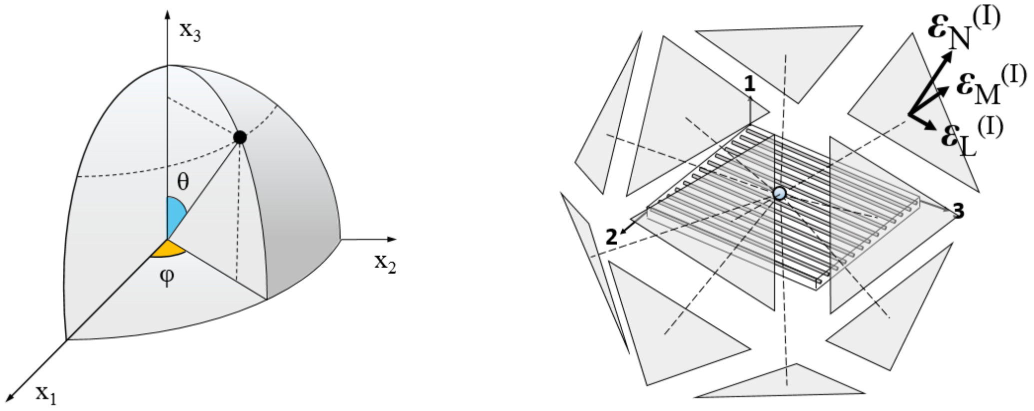

(a) (b)

Figure 2.1: Schematic representation of (a) a simple uni-directional composite cell with its local coordinate system and the microplanes used to define the constitutive laws of the material; (b) local spherical coordinate system.

The basic flow of the microplane material subroutine can be visualized in Fig. 2.2. The subroutine starts by reading in the input file generated by Abaqus, in which we define the boundary conditions such as boundary constraints and loading conditions in the direction of interest. In fact, the displacement loading defined in Abaqus is used as the strain in the macroscopic level and can be considered as the limit for which the element can be stretched in the defined time steps. Through the microplane subroutine, which acts as a material model, the strain vector on each microplane is projected through the P matrix such that

$$\boldsymbol{\varepsilon}_p = P\boldsymbol{\varepsilon} \tag{1}$$

where $\boldsymbol{\varepsilon}_p = [\varepsilon_N \quad \varepsilon_M \quad \varepsilon_L]^T$ is the strain vector on the microscopic planes, or microplane as illustrated in Fig. 2.1b and $\boldsymbol{\varepsilon}$ is the strain vector at the macroscopic level, which is defined by the user in Abaqus. Note that ε_N is the normal strain component and ε_M and ε_L are the tangential component. In addition,

$$P = \begin{bmatrix} N_{11} & N_{22} & N_{33} & \sqrt{2}N_{23} & \sqrt{2}N_{13} & \sqrt{2}N_{12} \\ M_{11} & M_{22} & M_{33} & \sqrt{2}M_{23} & \sqrt{2}M_{13} & \sqrt{2}M_{12} \\ L_{11} & L_{22} & L_{33} & \sqrt{2}L_{23} & \sqrt{2}L_{13} & \sqrt{2}L_{12} \end{bmatrix} \tag{2}$$

is a 3x6 projection matrix that relates the macroscopic strain tensor to the microplane strain vector as a function of the plane orientation denoted in Fig. 2.1a. Specifically, $N_{ij} = n_i n_j$, $M_{ij} = (m_i n_j + m_j n_i)/2$, and $L_{ij} = (l_i n_j + l_j n_i)/2$, where n_i, m_i, and l_i are local Cartesian coordinate vectors on the generic microplane with n_i being the i-th component of the normal. With reference to the spherical coordinate system represented in Fig. 2.1a, the foregoing components can be expressed as a function of the spherical angle θ and ϕ such that $n_1 = \sin\theta\cos\phi$, $n_2 = \sin\theta\sin\phi$, $n_3 = \cos\theta$, $m_1 = \cos\theta\cos\phi$, $m_2 = \cos\theta\sin\phi$, $m_3 = -\sin\theta$, $l_1 = -\sin\phi$, $l_2 = \cos\phi$, and $l_3 = 0$.

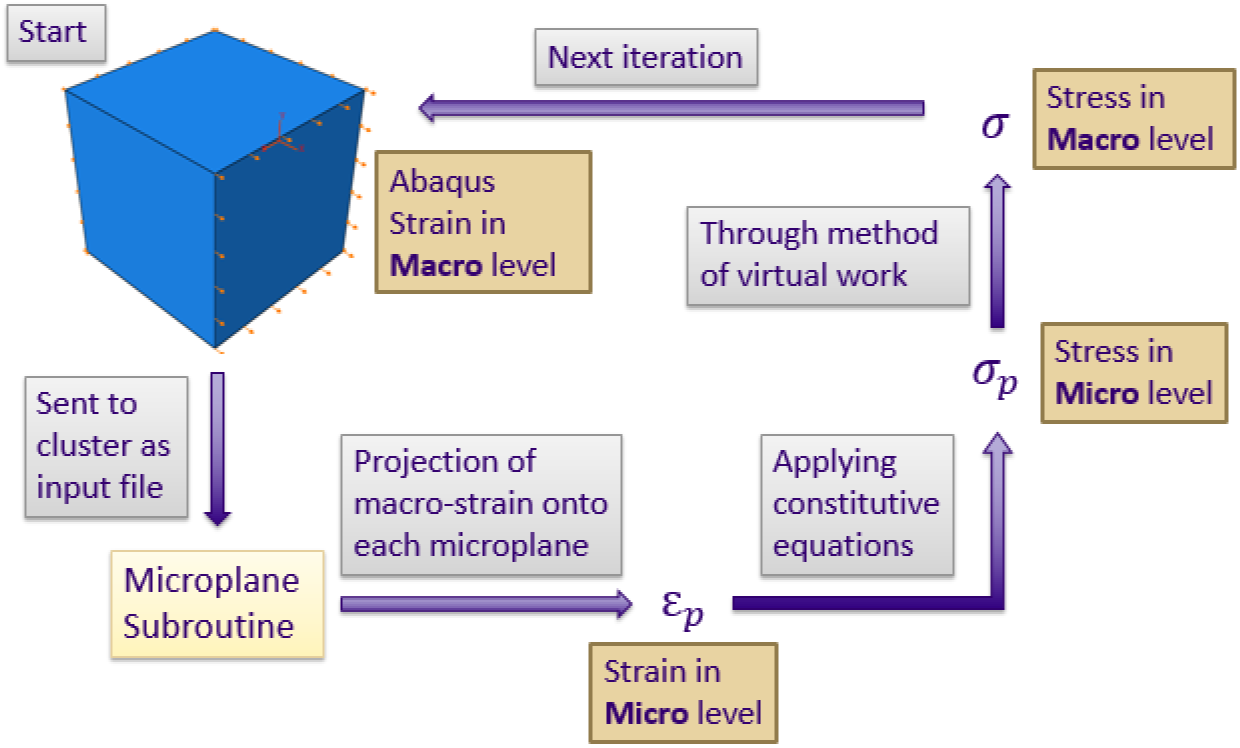

Fig 2.2: Flow chart of the microplane subroutine

Once the strain vector of the microplane is obtained, the subroutine calculates the corresponding microscopic stresses $\boldsymbol{\sigma}_p$ through the constitutive equations, which will be presented in detail in chapter 4. After the microplane stress vector $\boldsymbol{\sigma}_p$, the macroscopic stress tensor is defined in a variational sense through the principle of virtual work as:

$$\sigma = \frac{3}{2\pi}\int_{\Omega} P^T\, \boldsymbol{\sigma}_p d\Omega \tag{3}$$

where Ω is the surface of a hemisphere representing all the possible microplane orientations. Finally, the subroutine relates the macroscopic stress tensor to the macroscopic strain tensor, which is then used as the boundary condition for the next iteration of the simulation and the same procedure is repeated for the subsequent run until the desired number of step is reached.

2.3 BENEFITS OF MICROPLANE

Like mentioned in the previous section, the key feature of the microplane model is that the constitutive equations are related in terms of stress and strain vectors as opposed to stress and strain tensors in traditional tensorial constitutive models. By formulating the equations with this approach, a number of advantages are achieved. (1) The fact that the stresses and strains are presented in vectorial form significantly simplifies the complexity of the relations. Instead of having to deal with a 3x3 matrix, vectors comprised of just three entries are much simpler to work with. (2) Various physical phenomena are easier to formulate, thanks to the nature of vectorial constitutive description. Specifically, with microplanes oriented in different direction within the microstructure, it allows us to gain a better insight on the failure mechanism occurred in the microscopic level, for which the tensorial constitutive models are not capable of doing. With this feature, the analyst would have a better idea of the behavior of the material under certain kinds of loading and can use this failure information to predict and calculate the progressive energy dissipation upon reaching the elastic limit. (3) The model automatically exhibits the vertex effect, which is not captured by any of the practically usable tensorial models. (4) Interaction of microplanes provides all the cross-effects such as shear dilatancy and pressure sensitivity.

The penalty to pay for these advantages is an increased amount of computations. However, this penalty is becoming insignificant for the computers in the recent decade. Besides, the larger the system, the smaller the penalty due to the fact that large systems are computationally dominated by the structural stiffness matrix rather than the constitutive subroutine.

Chapter 3

Microplane Model with Spectral Decomposition Theorem

Until thus far, the microplane framework discussed has been general and is only applicable to generally isotropic materials such as traditional metals and concrete whose material properties are not direction-dependent. For composite materials, the material properties depend heavily on the direction of analysis such as the longitudinal (fibers) or transverse (matrix) direction as their elastic properties can be as far as ten folds in terms of numerical values. Therefore, to address the material's anisotropic characteristic, we decompose the stress and strain tensors into different energetically orthogonal modes through the spectral decomposition theorem. The following sections are intended to provide an introduction to the theorem.

3.1 SPECTRAL DECOMPOSITION OF THE ELASTIC TENSOR

The elastic behavior of a general anisotropic material can be expressed in Kelvin notation [15][16] as:

$$\boldsymbol{\sigma} = C\boldsymbol{\varepsilon} \tag{4}$$

where $\boldsymbol{\sigma} = \begin{bmatrix} \sigma_{11} & \sigma_{22} & \sigma_{33} & \sqrt{2}\sigma_{23} & \sqrt{2}\sigma_{13} & \sqrt{2}\sigma_{12} \end{bmatrix}^T$ and $\boldsymbol{\varepsilon} = \begin{bmatrix} \varepsilon_{11} & \varepsilon_{22} & \varepsilon_{33} & \sqrt{2}\varepsilon_{23} & \sqrt{2}\varepsilon_{13} & \sqrt{2}\varepsilon_{12} \end{bmatrix}^T$ are the contracted forms of the stress and strain second-order tensors and C represents the contracted form of the fourth-order elastic tensor. The indices refer to Cartesian coordinates x_i $(i = 1, 2, 3)$ as defined in Fig. 2.1. The factor $\sqrt{2}$ assures that both the stiffness tensor and its column matrix have the same norm, given by the sum of the squares of their elements.

By exploiting the spectral decomposition theorem, the compliance matrix S can be decomposed as follows:

$$S = \sum_I C^{(I)}\,\lambda^{(I)} \tag{5}$$

where $I = 1, 2, \dots 4$, λ_I are the eigenvalues of the compliance matrix and $S^{(I)} = \sum_n \phi_{In}\phi_{In}^T$ are set of second-order tensors constructed from the elastic eigenvectors ϕ_I. For the repeated eigenvalues or multiplicity greater than one, their corresponding eigenvectors ϕ is normalized such that

$$\phi_I^T C^{(I)}\phi_I = \lambda^{(I)} \tag{6}$$

to ensure orthogonality holds. In addition, the elastic eigenvalues and eigenmatrices can be found by treating the following as a general eigenvalue problem:

$$\det(\mathbf{S} - \lambda\mathbf{I}) = 0 \tag{7}$$

where the number of independent elastic eigenvalues is strictly related to the degree of anisotropy of the material. Furthermore, according to the spectral decomposition theorem, it is worth mentioning that the eigenmatrices $C^{(I)}$ have the following properties:

$$\text{partition of unity: } \sum_I C^{(I)} = I$$

$$\text{orthogonality: } C^{(I)}C^{(J)} = 0 \text{ if } I \neq J$$

$$\text{idempotent: } C^{(I)}C^{(I)} = C^{(I)}$$

The importance of the elastic eigenmatrices $C^{(I)}$ is that they provide a way to decompose the stress and strain tensors into energetically orthogonal modes, which are called eigenstresses and eigenstrains, respectively, and are defined as follows:

$$\boldsymbol{\sigma}_I = C^{(I)}\boldsymbol{\sigma} \tag{8}$$

$$\boldsymbol{\varepsilon}_I = C^{(I)}\boldsymbol{\varepsilon} \tag{9}$$

It is easy to show that $\boldsymbol{\sigma} = \sum_I \boldsymbol{\sigma}_I$ and $\boldsymbol{\varepsilon} = \sum_I \boldsymbol{\varepsilon}_I$. Further, through the relations between the eigenstresses and eigenstrains, one can conclude that $\boldsymbol{\sigma}_I = \lambda^{(I)} \boldsymbol{\varepsilon}_I$.

3.2 DECOMPOSITION FOR UNI-DIRECTIONAL COMPOSITE

The material under current study is the Silenka glass fiber 1200tex with MY750/HY917/DY063 epoxy. The elastic properties of the material can be found in Table 3.1 with a simple schematic representation as seen in Fig. 2.1b. We introduce a Cartesian coordinate system whose axis x_3 coincides with the direction of the fiber while x_1 and x_2 represent the transverse or the matrix direction. As can be noted from the figure, due to the planes of symmetry, specifically plane 1-2, 1-3, and 2-3 represent three planes of symmetry so that the material can be considered as orthotropic.

For a generic orthotropic material, the number of independent elastic constants is nine. In the case of a uni-directional composite, however, with the in-plane elastic moduli, out-of-plane Poisson's ratios and shear moduli are almost identical, it is prudent to further reduce the number of independent elastic constants to just five, making it a transversely isotropic material. The resulting material compliance matrix S can be expressed as follows:

$$S = \begin{bmatrix} 1/E_T & -\nu_T/E_T & -\nu_L/E_T & 0 & 0 & 0 \\ -\nu_T/E_T & 1/E_T & -\nu_L/E_T & 0 & 0 & 0 \\ -\nu_L/E_T & -\nu_L/E_T & 1/E_L & 0 & 0 & 0 \\ 0 & 0 & 0 & 1/2G_L & 0 & 0 \\ 0 & 0 & 0 & 0 & 1/2G_L & 0 \\ 0 & 0 & 0 & 0 & 0 & \frac{1+\nu_T}{E_T} \end{bmatrix} \tag{10}$$

where subscript T stands for properties in the transverse direction and L stands for properties in the longitudinal sense. The elastic stiffness matrix can be determined as $C = S^{-1}$.

Table 3.1: Experimental elastic properties of Silenka glass fiber composite.

Material property	Symbol	Literature values (unit)
Elastic modulus (fiber)	$E_L = E_3$	45600 (MPa)
Elastic modulus (matrix)	$E_L = E_1 = E_2$	11000 (MPa)
In-plane shear modulus	$G_L = G_{13} = G_{23}$	6600 (MPa)
Out-of-plane shear modulus	$G_T = G_{12}$	3928.6 (MPa)
In-plane Poisson's ratio	$\nu_L = \nu_{13} = \nu_{23}$	0.0244 (-)
Out-pf-plane Poisson's ratio	$\nu_T = \nu_{12}$	0.4 (-)

With the material symmetry, the closed form solution of the elastic eigenvalue problem presented in Eq. (7) can be calculated and the following four independent elastic eigenvalues can be obtained:

$$\lambda^{(1)^{-1}} = \frac{1+\nu_T}{E_T}$$

$$\lambda^{(2)^{-1}} = \frac{1-\nu_T}{2E_T} + \frac{1}{2E_L} + \left[\left(\frac{1-\nu_T}{2E_T} - \frac{1}{2E_L}\right)^2 + \frac{2\nu_L^2}{E_T^2}\right]^{1/2}$$

$$\lambda^{(3)^{-1}} = \frac{1-\nu_T}{2E_T} + \frac{1}{2E_L} - \left[\left(\frac{1-\nu_T}{2E_T} - \frac{1}{2E_L}\right)^2 + \frac{2\nu_L^2}{E_T^2}\right]^{1/2}$$

$$\lambda^{(4)^{-1}} = \frac{1}{2G_L} \tag{11}$$

Note that they are the inverted eigenvalues since we are working with the material's compliance matrix. Their corresponding eigenmatrix, constructed from the normalized eigenvectors in Eq. (6) are as follows:

$$C^{(1)} = \begin{bmatrix} 1/2 & -1/2 & 0 & 0 & 0 & 0 \\ -1/2 & 1/2 & 0 & 0 & 0 & 0 \\ 0 & 0 & 0 & 0 & 0 & 0 \\ 0 & 0 & 0 & 0 & 0 & 0 \\ 0 & 0 & 0 & 0 & 0 & 0 \\ 0 & 0 & 0 & 0 & 0 & 1 \end{bmatrix}$$

$$C^{(2)} = \begin{bmatrix} c^2/2 & c^2/2 & cs/\sqrt{2} & 0 & 0 & 0 \\ c^2/2 & c^2/2 & cs/\sqrt{2} & 0 & 0 & 0 \\ cs/\sqrt{2} & cs/\sqrt{2} & s^2 & 0 & 0 & 0 \\ 0 & 0 & 0 & 0 & 0 & 0 \\ 0 & 0 & 0 & 0 & 0 & 0 \\ 0 & 0 & 0 & 0 & 0 & 0 \end{bmatrix}$$

$$C^{(3)} = \begin{bmatrix} s^2/2 & s^2/2 & -cs/\sqrt{2} & 0 & 0 & 0 \\ s^2/2 & s^2/2 & -cs/\sqrt{2} & 0 & 0 & 0 \\ -cs/\sqrt{2} & -cs/\sqrt{2} & c^2 & 0 & 0 & 0 \\ 0 & 0 & 0 & 0 & 0 & 0 \\ 0 & 0 & 0 & 0 & 0 & 0 \\ 0 & 0 & 0 & 0 & 0 & 0 \end{bmatrix}$$

$$C^{(4)} = \begin{bmatrix} 0 & 0 & 0 & 0 & 0 & 0 \\ 0 & 0 & 0 & 0 & 0 & 0 \\ 0 & 0 & 0 & 0 & 0 & 0 \\ 0 & 0 & 0 & 1 & 0 & 0 \\ 0 & 0 & 0 & 0 & 1 & 0 \\ 0 & 0 & 0 & 0 & 0 & 0 \end{bmatrix} \tag{12}$$

where $c = \cos\omega$ and $s = \sin\omega$ and ω, interpreted as the eigenangle is defined as:

$$\omega = \frac{1}{2}\tan^{-1}\left(\frac{-2\sqrt{2}\,\frac{\nu_L}{E_T}}{\frac{(1-\nu_T)}{E_T} - \frac{1}{E_L}}\right)$$

We can see that for a generic uni-directional material matrix, four orthogonal modes are obtained. Each mode governs the material behaviors in such a way that some describes the loading in the fiber direction while the others control the matrix and shear loading conditions. These orthogonal modes are also referred as material's eigenmodes, for which we will examine more closely in the next section.

3.3 MICROPLANE EIGENSTRAIN DISTRIBUTION

With the aid of spectral decomposition theorem and keeping the microplane orientation in general, we are able to obtain the analytical expressions for the normal $\varepsilon_N^{(I)}$ and the shear components $\varepsilon_M^{(I)}$ and $\varepsilon_L^{(I)}$ of the microplanes by substituting Eq. (2) and Eq. (12) into the following equations:

$$\boldsymbol{\varepsilon}_p = \sum_I^N \boldsymbol{\varepsilon}_p^{(I)} \quad \text{where} \quad \begin{cases} \boldsymbol{\varepsilon}_p^{(I)} = P\varepsilon^{(I)} = P^{(I)}\varepsilon \\ P^{(I)} = PC^{(I)} \end{cases} \tag{13}$$

where N is the number of independent eigenmodes.

Table 3.2: Microplane strain modes – normal components

Mode	ε_N
1	$\sin^2\theta\left[\alpha_1(\cos^2\phi - \sin^2\phi) + 2\sqrt{2}\varepsilon_6 \sin\phi\cos\phi\right]$
2	$\alpha_2\left(\cos\omega\sin^2\theta/\sqrt{2} + \sin\omega\ \cos^2\theta\right)$
3	$\alpha_3\left(-\sin\omega\sin^2\theta/\sqrt{2} + \cos\omega\ \cos^2\theta\right)$
4	$2\sqrt{2}\sin\theta\cos\theta\ (\varepsilon_4\sin\phi + \varepsilon_5\cos\phi)$

Table 3.3: Microplane strain modes – tangential components

Mode	ε_M
1	$\sin\theta\cos\theta\left[\alpha_1(\cos^2\phi-\sin^2\phi)+2\sqrt{2}\varepsilon_4\sin\phi\cos\phi\right]$
2	$\alpha_2\sin\theta\cos\theta\left(\cos\omega/\sqrt{2}-\sin\omega\right)$
3	$\alpha_3\sin\theta\cos\theta\left(-\sin\omega/\sqrt{2}-\cos\omega\right)$
4	$\sqrt{2}(\cos^2\theta-\sin^2\theta)(\varepsilon_4\sin\phi+\varepsilon_5\cos\phi)$
Mode	ε_L
1	$\sin\theta\left[\alpha_1\sin\phi\cos\phi+\sqrt{2}\varepsilon_6(\cos^2\phi-\sin^2\phi)\right]$
2	0
3	0
4	$\sqrt{2}\cos\theta(\varepsilon_4\cos\phi-\varepsilon_5\sin\phi)$

where $\alpha_1=(\varepsilon_1-\varepsilon_2)/2, \alpha_2=\cos\omega\,(\varepsilon_1+\varepsilon_2)/2+\varepsilon_3\sin\omega$ and $\alpha_3=-\sin\omega\,(\varepsilon_1+\varepsilon_2)/2+\varepsilon_3\cos\omega$. As noted from the analytical expressions above, the microplane strain components depend on the applied macroscopic strains as well as the orientation of microplane embedded in the eigenangle ω.

Let us now take a closer look at the distribution of the normal strain components on the microplane sphere caused by a uniaxial strain applied at the macroscopic level in the longitudinal or the fiber direction (x_3 axis) such that $\varepsilon=[0\quad 0\quad 1\quad 0\quad 0\quad 0]^T$ (Fig. 3.1). Strain mode 1 and 4 are equal to zero because they do not depend on ε_3 whereas strain mode 2 and 3 are nonzero. From Fig. 3.1a, with the orange dashed circle being the undeformed microplane distribution, it is clear that for mode 3, the microplanes oriented perpendicularly to the fiber direction experience the greatest change in strain while the ones that lie in the matrix direction only deform a small amount. If following the same procedure with the same applied macroscopic strain and examine mode 2, we see that the microplane strain distribution is also deformed, but with a negligible amount in comparison to mode 3. This interaction is due to that mode 2 is not completely independent of ε_3 and this small amount of change in strain in mode 2 will play a significant role later on in the calibration process. From this analysis, we can conclude that mode 3 governs the fiber behavior of the composite material.

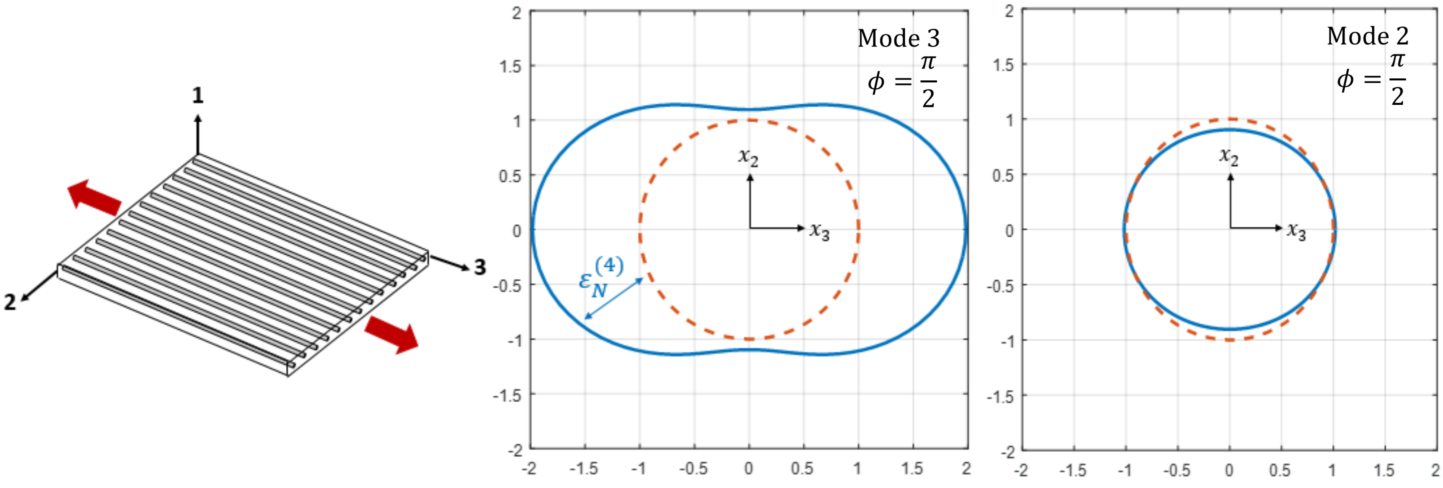

(a) (b)

Figure 3.1: Distribution of the normal microplane strain related to (a) mode 3, (b) mode 2 in the presence of a uniaxial macroscopic strain in the longitudinal or $x_3$direction

Same procedure is then carried out to examine the behavior of other modes with the uniaxial strain applied along the transvers or the matrix direction (x_1 and x_2), as can be seen in Fig. 3.2. According to Table 3.2 above, mode 4 will be zero because its indifference of ε_1 and ε_2 whereas mode 3 has negligible effect compared to both mode 1 and 2. As seen from the figures, one can reach the conclusion that mode 2 behaves as the deviatory mode, loading mainly the microplanes whose normal is close to the direction of application of the macroscopic strain. Conversely, mode 1 governs the volumetric behavior of the matrix, as the deformation is uniformly distributed along the 2-3 plane. In addition, since both modes 1 and 2 describe the uniaxial behavior of the plane of matrix, it is convenient to consider the effect of the two modes together and name it mode 12, which has strong matrix-dominated properties. By doing so helps reduce the number of parameter during the calibration phase. It also helps preserve the physical intuition of the material in such a way that now there is one single mode that controls the behavior of the matrix material within the composite rather than having two.

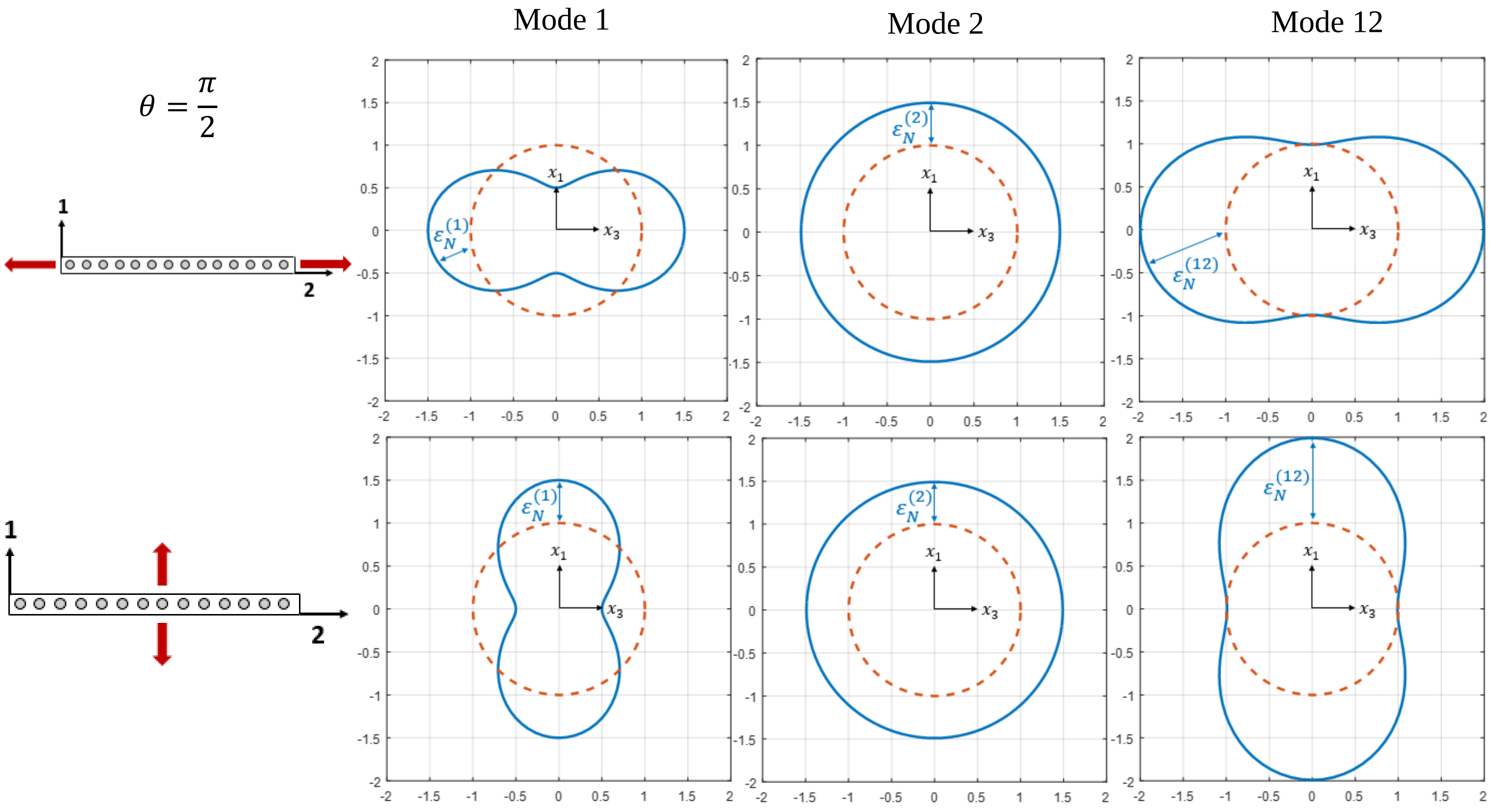

(a) (b) (c)

Figure 3.2: Distribution of the normal microplane strain related to (a) mode 1, (b) mode 2, and (c) mode 12 in the presence of a uniaxial macroscopic strain in plane 1-2.

Similarly, for the in-plane shear mode or mode 4, it is only activated in the presence of macroscopic strain ε_5. In this configuration, all other modes are zero because the shear mode is completely decoupled from all of them while mode 4 acts mainly on microplanes oriented in direction $\theta = \pi/4$, as can be seen in Fig. 3.3. Like mode 1 and 2, the in-plane shear behavior is highly dictated by the matrix as it can be considered as a matrix-dominated mode.

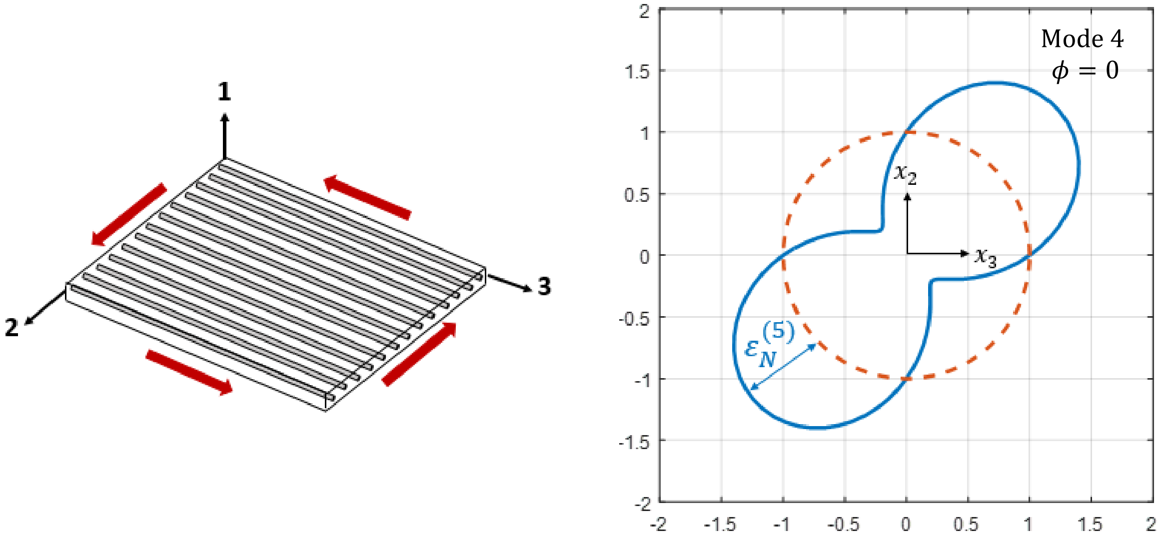

Figure 3.3: Distribution of the normal microplane strain related to mode 4 in the presence of a macroscopic in-plane shear strain.

Chapter 4

Material calibration and validation

Thus far in this study, a three-dimensional constitutive model for transversely isotropic composite laminates has been proposed in the microplane framework. The formulation exploits the spectral decomposition of the orthotropic stiffness matrix to decompose the strain tensor into four orthogonal strain modes. Strain mode 1 and 2 govern the transverse behavior, for which is matrix-dominated, mode 3 governs the longitudinal behavior, which has fiber-dominated properties, and mode 4 determines the shear behavior of the material.

In the following section, the model will be calibrated and validated by comparing numerical results to published experimental data for uniaxial tests. Simulations of the behavior of unidirectional glass-epoxy laminates will be compared against with the experimental data reported in [17]. As the following calibration analysis, it can be seen that in the elastic regime, the four strain modes can be considered to be decoupled from each other, however, in the inelastic regime a certain degree of coupling is necessary to achieve good fit of the experimental results.

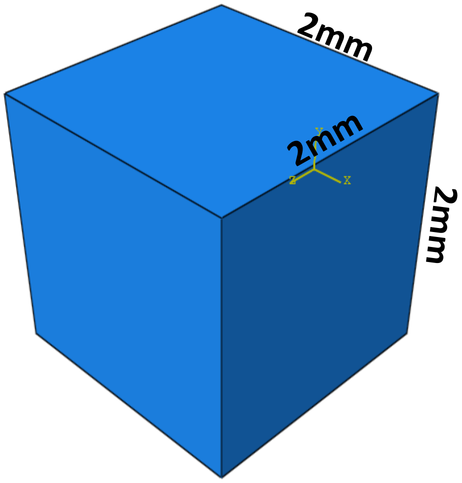

Figure 4.1: Schematic representation of the 2mm cube used in calibration

4.1 UNIAXIAL STRESS STRAIN CURVES OF UNI-DIRECTIONAL LAMINATES

The calibration procedure consists of two steps for each of the eigenmodes obtained in section 3.2: First, parameters governing the pre-peak phase are adjusted to match the elastic portion of the experimental stress-strain curves reported in literature. After which, since the inelastic portion of the stress strain curve is often not reported in literatures, the post-peak regime is calibrated by adjusting the softening parameters to match the fracture energy under the curve. The reason that the softening part of the curve is usually unavailable is due to the fact that material undergoes the snapback effect upon its yielding in the experiments. Snapback effect occurs when the material reaches its elastic stress limit as the stress travels backwards with decreasing strain. Therefore, the calibration effort is shifted toward matching the fracture energy, which is also not readily available in the literatures. However, educated guess based on a recent study on size effects of composite material [2], [18] is utilized to come up with a rough estimate for calibration purposes. In the current calibration procedure, a $h = 2mm$ cube is considered based on adequately fitting results with other material [18]. A simple schematic of the cube constructed in Abaqus is shown in Fig. 4.1.

The spectral stiffness microplane model aims at representing the main physical mechanisms characterizing the material's behavior in the macroscopic level by capturing the material's behavior through microplanes projected in the microscopic level. To start the calibration process and formulate the constitutive equations for each mode, the equivalent strain for the microplane must be first obtained. As discussed earlier, for a generic Ith eigenmodes, the microplane strain vector is computed using the projection matrix P shown in Eq. (2), the corresponding eigenmatrix C from Eq. (12), and the applied macroscopic strain $\boldsymbol{\varepsilon}$. The equivalent microplane strain is nothing but the resultant of the three strain components as follows:

$$\varepsilon_p^I = \begin{Bmatrix} \varepsilon_N \\ \varepsilon_M \\ \varepsilon_L \end{Bmatrix}^I = PC^{(I)}[\varepsilon_1 \quad \varepsilon_2 \quad \varepsilon_3 \quad \varepsilon_4 \quad \varepsilon_5 \quad \varepsilon_6]^T \tag{14}$$

$$\varepsilon^{(I)} = \sqrt{\left(\varepsilon_N^{(I)}\right)^2 + \left(\varepsilon_M^{(I)}\right)^2 + \left(\varepsilon_L^{(I)}\right)^2} \tag{15}$$

The constitutive laws can then be defined by means of an effective microplane eigenstress $\sigma^{(I)}$. The relation between the microscopic stresses and macroscopic stresses can be found by imposing the method of virtual work:

$$\begin{aligned} \delta W_1 = \sigma^{(I)}\delta\varepsilon^{(I)} &= \frac{\sigma^{(I)}}{\varepsilon^{(I)}}(\varepsilon_N\delta\varepsilon_N + \varepsilon_M\delta\varepsilon_M + \varepsilon_L\delta\varepsilon_L)^{(I)} \\ &= (\varepsilon_N\delta\varepsilon_N)^{(I)} + (\varepsilon_M\delta\varepsilon_M)^{(I)} + (\varepsilon_L\delta\varepsilon_L)^{(I)} \end{aligned} \tag{16}$$

It should be noted that, thanks to the definition in Eq. (14) and (15) and to Eq. (16), $\delta W_1 \geq 0$ for all microplanes. This entails that energy dissipation on each microplane is non-negative, a condition to fulfill the second law of thermodynamics.

By means of Eq. (16), the relationship between normal and shear stresses versus normal and shear strains can be formulated through damage-type constitutive equations:

$$\sigma_N^{(1)} = \left(\sigma\frac{\varepsilon_N}{\varepsilon}\right)^{(I)} \qquad \sigma_M^{(1)} = \left(\sigma\frac{\varepsilon_M}{\varepsilon}\right)^{(I)} \qquad \sigma_L^{(1)} = \left(\sigma\frac{\varepsilon_L}{\varepsilon}\right)^{(I)} \tag{17}$$

It is worth pointing out that, substituting and rearranging Eq. (17) into (14) and (15) can lead to the following definition of the I$^{\text{th}}$ effective stress:

$$\sigma^{(I)} = \sqrt{\left(\sigma_N^{(I)}\right)^2 + \left(\sigma_M^{(I)}\right)^2 + \left(\sigma_L^{(I)}\right)^2} \tag{18}$$

4.2 Calibration and Validation: Shear Mode

Let us first consider the laminate behavior under shear loading. In this type of deformation, the material undergoes an extensive micro-cracking before reaching the elastic limit, which produces a unique nonlinear behavior. In order to capture this phenomenon, the relation between stress and strain can be expressed as follows:

$$\sigma_T^{(4)} = \left(s^{(4)}\right)^{1-p}\left(\lambda^{(4)}\right)^p \begin{cases} \varepsilon^p & \text{if } \varepsilon \leq \frac{s^{(4)}}{\lambda^{(4)}} \\ \left(k_{at}^{(4)}\right)^p \langle 1 - \frac{\varepsilon - k_{at}^{(4)}}{k_{bt}^{(4)}} \rangle & \text{if } \varepsilon > \frac{s^{(4)}}{\lambda^{(4)}} \end{cases} \tag{19}$$

for $\varepsilon_N^{(4)} \geq 0$ and

$$\sigma_C^{(4)} = \left(c^{(4)}\right)^{1-p}\left(\lambda^{(4)}\right)^p \begin{cases} \varepsilon^p & \text{if } \varepsilon \leq \frac{c^{(4)}}{\lambda^{(4)}} \\ \left(k_{ac}^{(4)}\right)^p \langle 1 - \frac{\varepsilon - k_{ac}^{(4)}}{k_{bc}^{(4)}} \rangle & \text{if } \varepsilon > \frac{c^{(4)}}{\lambda^{(4)}} \end{cases} \tag{20}$$

for $\varepsilon_N^{(5)} < 0$. The function $s^{(4)}(\theta, \phi) = s_0^{(4)}$and $c^{(4)}(\theta, \phi) = c_0^{(4)}$ represent mode 4 microplane tensile and compressive stresses at which non-linearity starts and they are both assumed to be independent of the microplane orientation. p is a parameter controlling the slope of the curve in the pre-peak region and is assumed to be the same in tension and compression. The parameters $k_{at}^{(4)}$ and $k_{ac}^{(4)}$ represent the value of the effective strain at the beginning of the linear softening region whereas the parameters $k_{bt}^{(4)}$ and $k_{bc}^{(4)}$ determine the softening strain value at which $\sigma = 0$ in tension and compression, respectively.

The experimental data available for this loading condition is the stress-strain curve up to the elastic limit, in-plane shear strength $s = 73$MPa and in-plane shear failure strain $\varepsilon = 4\%$. The calibration process begins by adjusting the value of $s^{(4)}$ and p so to match the experimental data in the elastic region. It should be noted that the value of $s^{(4)}$ and the reported value of s from literature are the strength for the microscopic and macroscopic level, respectively.

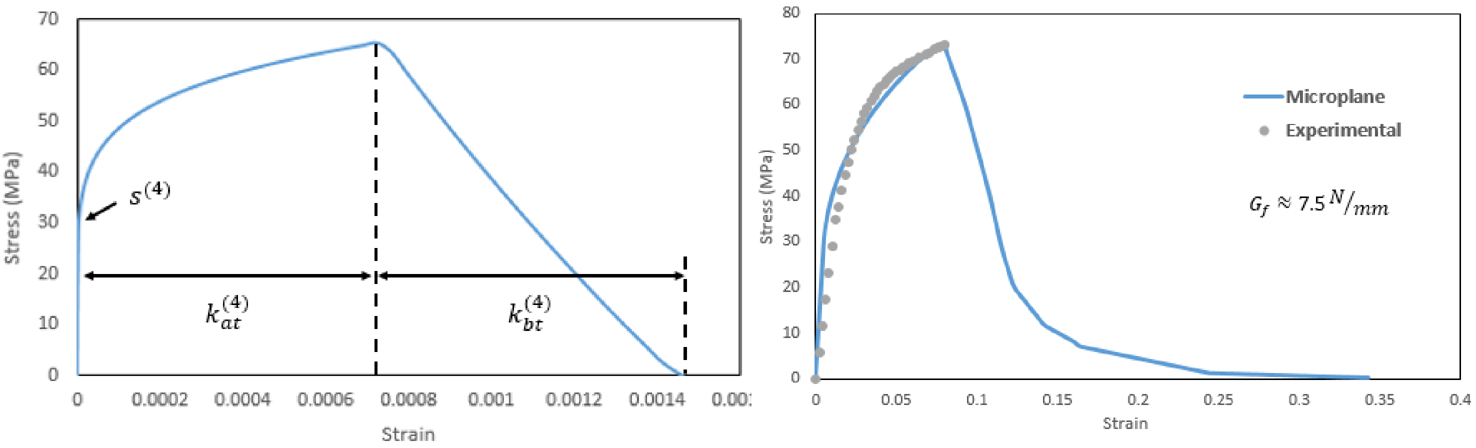

(a) (b)

Figure 4.2: Shear loading of (a) Stress-strain boundary for microplane constitutive law. (b) Stress-strain curve for the overall composite laminate with experimental data.

Once the pre-peak region matches with the reported stress-strain curve, the value of $k_{bt}^{(4)}$ is then adjusted in order to finish the calibration. As mentioned above, parameter $k_{bt}^{(4)}$ determines the equivalent strain value of the softening regime. This portion of the calibration is done by adjusting $k_{bt}^{(4)}$ so that the area under the stress-strain curve or the fracture energy matches with our target value. According to the analyses performed in the recent study [2], the value of fracture energy under shear loading for uni-directional composite can be estimated to be about 8 ${}^{N}/_{mm}$ as our simulation yielded an area of 7.5 ${}^{N}/_{mm}$, which falls within the expectation.

Fig. 4.2 illustrates the stress-strain curves for (a) one of the infinite microplanes and (b) the macroscopic behavior of the overall composite laminate. We can see that from (a), upon reaching the stress limit $s^{(4)}$, the matrix undergoes micro-cracking and is resulted in a nonlinear behavior, defined by parameter p, up to the elastic limit, for which the corresponding strain value is defined by $k_{at}^{(4)}$. As the laminate passes the yield point, softening occurs and the material does so in a nonlinear fashion which is controlled by the parameter $k_{bt}^{(4)}$.

In cases in which the macroscopic shear behavior is independent of the sign of the deformation, the same parameters at microscopic level can be used in both tension and compression. Therefore, for the present study, the number of required parameter is four instead of seven, as reported in Table 4.1.

Table 4.1: Calibration parameters for shear loading conditions

Description	Symbol (units)	Calibrated value
Mode 4 elastic eigenvalue	$\lambda^{(4)}$ (MPa)	11660
Microplane peak stress in tension	$s_0^{(4)}$ (MPa)	29
Exponent governing non-linearity in tension and compression	p (-)	0.3
Strain at starting of post-peak softening in tension	$k_{at}^{(4)}$ (-)	0.038
Parameter governing post-peak softening in tension	$k_{bt}^{(4)}$ (-)	0.015
Microplane peak stress in compression	$c_0^{(4)}$ (MPa)	29
Strain at starting of post-peak softening in compression	$k_{ac}^{(4)}$ (-)	0.038
Parameter governing post-peak softening in compression	$k_{bc}^{(4)}$ (-)	0.015

4.3 CALIBRATION AND VALIDATION: MATRIX MODE

As discussed in section 3.3, since both mode 1 and 2 describe the matrix behavior in the presence of a macroscopic uniaxial in the transverse direction, it is convenient to combine them together. To ensure the combined mode yields correct results, the following expressions are introduced to accommodate the change in microplane strain:

$$\varepsilon_{N12} = \varepsilon_{N1}\frac{\lambda_1}{\lambda_2} + \varepsilon_{N2} \qquad \varepsilon_{M12} = \varepsilon_{M1}\frac{\lambda_1}{\lambda_2} + \varepsilon_{M2} \qquad \varepsilon_{L12} = \varepsilon_{L1}\frac{\lambda_1}{\lambda_2} + \varepsilon_{L2} \tag{21}$$

the equivalent strain is calculated the same way as before, such that:

$$\varepsilon_{12} = \sqrt{{\varepsilon_{N12}}^2 + {\varepsilon_{M12}}^2 + {\varepsilon_{L12}}^2} \tag{22}$$

The virtual work can be calculated as done in Eq. (16):

$$\delta W_{12} = \frac{\sigma^{(12)}}{\varepsilon^{(12)}} \left[\frac{\lambda^{(1)}}{\lambda^{(2)}} \left(\varepsilon_N^{(1)} \delta\varepsilon_N^{(1)} + \varepsilon_M^{(1)} \delta\varepsilon_M^{(1)} + \varepsilon_L^{(1)} \delta\varepsilon_L^{(1)} \right) + \varepsilon_N^{(2)} \delta\varepsilon_N^{(2)} + \varepsilon_M^{(2)} \delta\varepsilon_M^{(2)} + \varepsilon_L^{(2)} \delta\varepsilon_L^{(2)} \right] \tag{23}$$

Now, the relationship between normal and shear stresses versus normal and shear strains can be formulated through the following damage-type constitutive equations:

$$\sigma_N^{(12)} = \frac{\sigma^{(12)}}{\varepsilon^{(12)}} \left(\frac{\lambda^{(1)}}{\lambda^{(2)}} \varepsilon_N^{(1)} + \varepsilon_N^{(2)} \right) \qquad \sigma_M^{(12)} = \frac{\sigma^{(12)}}{\varepsilon^{(12)}} \left(\frac{\lambda^{(1)}}{\lambda^{(2)}} \varepsilon_M^{(1)} + \varepsilon_M^{(2)} \right)$$

$$\sigma_L^{(12)} = \frac{\sigma^{(12)}}{\varepsilon^{(12)}} \left(\frac{\lambda^{(1)}}{\lambda^{(2)}} \varepsilon_L^{(1)} + \varepsilon_L^{(2)} \right) \tag{24}$$

Again, combining Eq. (24) with Eq. (21) and (22), one is able to obtain the new definition of the effective stress:

$$\sigma^{(12)} = \sqrt{\frac{\lambda^{(2)}}{\lambda^{(1)}} \left[\left(\sigma_N^{(1)} \right)^2 + \left(\sigma_T^{(1)} \right)^2 \right] + \left(\sigma_N^{(2)} \right)^2 + \left(\sigma_T^{(2)} \right)^2} \tag{25}$$

With the equivalent stress and strain defined for the new combined mode, let us define the constitutive equations for the transverse loading direction:

$$\sigma_T^{(12)} = \begin{cases} \varepsilon_{12} \cdot \lambda^{(2)} & \text{if} \quad \varepsilon_{12} \leq \frac{s_0^{(12)}}{\lambda^{(2)}} \\ s_0^{(12)} \left(\frac{1 - \left(\varepsilon - \frac{s_0^{(12)}}{\lambda^{(2)}} \right)}{k_{bt}^{(12)}} \right) & \text{if} \quad \varepsilon_{12} > \frac{s_0^{(12)}}{\lambda^{(2)}} \end{cases} \tag{26}$$

for $\varepsilon_{N12} \geq 0$ and

$$\sigma_C^{(12)} = \begin{cases} \varepsilon_{12} \cdot \lambda^{(2)} & \text{if} \quad \varepsilon_{12} \leq \frac{c_0^{(12)}}{\lambda^{(2)}} \\ c_0^{(12)} \left(\frac{1 - \left(\varepsilon - \frac{c_0^{(12)}}{\lambda^{(2)}} \right)}{k_{bc}^{(12)}} \right) & \text{if} \quad \varepsilon_{12} > \frac{c_0^{(12)}}{\lambda^{(2)}} \end{cases} \tag{27}$$

for $\varepsilon_{N12} < 0$. $s_0^{(12)}$ and $c_0^{(12)}$ represent mode 12 microplane tensile and compressive strength, respectively. $k_{bt}^{(12)}$ and $k_{bc}^{(12)}$ are parameters that determine the effective strain in the softening region. Again, these constitutive equations describe the behaviors of the material under uniaxial loading in the transverse direction in the microscopic level and are constructed by two linear functions with one governing the pre-peak and the post-peak behavior. For instance, as the material subject to tension loading with the equivalent strain less than the value of $\frac{s_0^{(12)}}{\lambda^{(2)}}$, for which the result is a constant or the strain value at yielding point, the microplane will stay in the elastic regime and returns a linear line going up towards the peak stress. As this value is reached, meaning yielding has occurred, stress starts decreasing and the downwards slope is controlled by parameter $k_{bt}^{(12)}$, similar as in the shear cases. Likewise for the case under compressive loading, one difference is that the value of $c_0^{(12)}$ is negative.

With the aforementioned constitutive equation, however, an issue was encountered during the calibration process when loading happened in the fiber direction in that the stress limit was never reached for fiber regardless the parameters. The source of the problem was that since the elastic properties of fiber and matrix are so similar, matrix would always soften prior to the fiber, which resulted in a premature softening behavior in the stress-strain curve. As discussed in section 3.3, the fiber and matrix modes are not completely independent after the spectral decomposition theorem as there is still a negligible amount of strain observed in the transverse direction under uniaxial load applied in the longitudinal direction, as seen in Fig. 3.1b. It is worth mentioning that this interaction between these two modes are especially significant for the material under this study due to the fact that the elastic limit of fiber and matrix is so close. With a quick search online, one can observe that for carbon fiber composites, the ratio between Young's modulus of fiber and matrix can be well in the range of ten to fifteen as opposed to less than three for the material under current study. With similar elastic properties, it means less distinctive eigenvalues, which yield comparable stress and strains between the modes.

Therefore, a solution was proposed to address this issue by defining inequalities that set the boundary for the values of strength in which the matrix is allowed to soften. The following bounding equations are introduced:

$$\begin{aligned} s_{12}^{ct} &> \alpha - \beta(s_1)sign(\varepsilon_{N2}) \\ s_{12}^{cc} &< \alpha - \beta(s_1)sign(\varepsilon_{N2}) \end{aligned} \tag{28}$$

s_{12}^{ct} and s_{12}^{cc} are the critical strength for fiber in tension and compression, respectively, α and β are calibration parameters for the inequalities and the sign function extracts only the sign of its argument. The values of s_{12}^{ct} and s_{12}^{cc} are determined by examining the failure strength under tension and compression in the microscopic level for the element, and ε_{N2} is the corresponding failure strain, which is positive for tension and vice versa. With these values found, α and β cab be evaluated from the inequalities provided that there are two unknowns and two equations. The idea of Eq. (28) is to find α and β such that the inequalities never satisfy under uniaxial loading in the longitudinal direction. Specifically, during this loading condition, a nonzero strain is observed in the x_2 direction whereas the value of s_1 is always zero, meaning β does not play a role when a uniaxial load in fiber direction is in presence. Having this in mind, in order to not satisfy both inequalities in Eq. (28), the value of α needs to be in between s_{12}^{ct} and s_{12}^{cc}, where the former is larger because matrix can generally withstand high loads in compression.

With Eq. (28) implemented, the constitutive equations governing the matrix behaviors are modified and defined as follow:

$$\sigma_T^{(12)} = \begin{cases} \varepsilon_{12} \cdot \lambda^{(2)} & \text{if} \quad s_{12}^{ct} - \left(\alpha - \beta(s_1) sign(\varepsilon_{N2})\right) > 0 \\ s_{12}^{ct} \left(\dfrac{1 - \left(\varepsilon_{12} - \frac{s_{12}^{ct}}{\lambda^{(2)}}\right)}{k_{bt}^{(12)}} \right) & \text{if} \quad s_{12}^{ct} - \left(\alpha - \beta(s_1) sign(\varepsilon_{N2})\right) \leq 0 \end{cases} \tag{29}$$

$$\sigma_C^{(12)} = \begin{cases} \varepsilon_{12} \cdot -\lambda^{(2)} & \text{if} \quad s_{12}^{cc} - \left(\alpha - \beta(s_1) sign(\varepsilon_{N2})\right) < 0 \\ s_{12}^{cc} \left(\dfrac{1 - \left(\varepsilon_{12} - \frac{s_{12}^{cc}}{\lambda^{(2)}}\right)}{k_{bc}^{(12)}} \right) & \text{if} \quad s_{12}^{cc} - \left(\alpha - \beta(s_1) sign(\varepsilon_{N2})\right) \geq 0 \end{cases} \tag{30}$$

Eq. (29) and (30) effectively resolve the problem of premature softening for the composite material with a uniaxial strain in the fiber direction and they do not have any advert effect in terms of calibrating with loading occurs in the transverse direction.

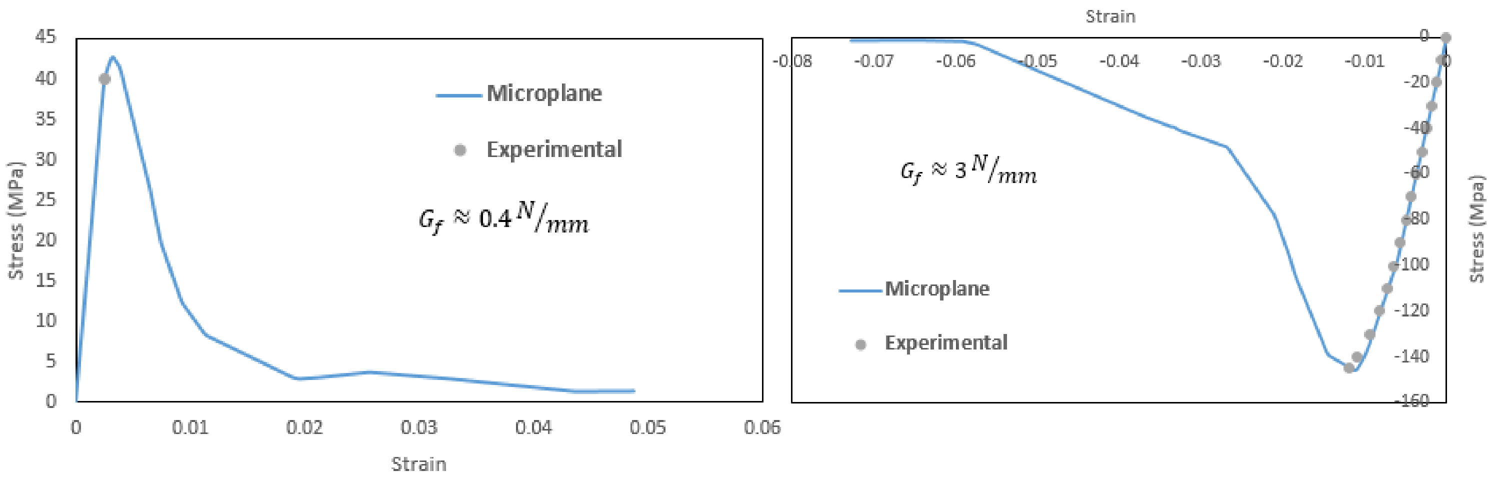

(a) (b)

Figure 4.3: Stress-strain curves of the composite laminate in the presence of uniaxial loading in (a) tension; (b) compression in the transverse direction.

The calibration process began with similar steps as in the shear mode. Effort was done in calibrating the values of s_{12}^{ct} and s_{12}^{cc} so that the pre-peak portion of the stress-strain curve matches the experimental data. As can be seen in Fig. 4.3, only one data point was reported for the tension test and the elastic part of the stress-strain curve for the compression test. The microplane model is able to have good fits with the experimental data for both loading cases. Similar steps were taken after matching the experimental data for the pre-peak region where $k_{bt}^{(12)}$ and $k_{bc}^{(12)}$ values were adjusted in order to match the fracture energy for the two cases. According to epoxy in general and from [2], $0.5\, {}^{N}/_{mm}$ and $3\, {}^{N}/_{mm}$ were the approximation for the fracture energy in tension and compression, respectively. The calibrated value of each parameter is presented in Table 4.2:

Table 4.2: Calibration parameters for transverse loading conditions

Description	Symbol (units)	Calibrated value
Mode 2 elastic eigenvalue	$\lambda^{(2)}$ (MPa)	26786
Calibration parameter	α	62.6947
Calibration parameter	β	1.45
Microplane peak stress in tension	s_{12}^{ct}	36
Microplane peak stress in compression	s_{12}^{cc}	133
Parameter governing post-peak softening in tension	$k_{bt}^{(4)}$ (-)	0.0026
Parameter governing post-peak softening in compression	$k_{bc}^{(4)}$ (-)	0.0035

4.4 CALIBRATION AND VALIDATION: FIBER MODE

As strain is introduced in the longitudinal direction, the nonlinear behavior is observed for the composite laminate when the matrix's elastic limit is reached, whose strength is significantly lower than that of the fibers. At this point, fibers are still within the elastic phase and, consequently, stresses can be redistributed in the microstructure, allowing an overall increase of the applied load. The maximum load carrying capacity of the composite is obtained upon the fibers fail. The fibers, however, do not fail simultaneously as most of the formulations predict, rather they fail in such a way that gradual reduction in stresses takes place in fibers as the strain increases, producing a nonlinear behavior in softening.

Thanks to the implementation of Eq. (29) and (30) in the code, interactions between the modes are subsided as the fibers can now be loaded up to its elastic limit without the premature softening caused by the matrix. The calibration effort is similar as before where parameters are adjusted to match the elastic portion prior to the softening regime. Specifically, the parameters of $s^{(4)}$ and $c^{(4)}$ are the tensile and compressive strength in the longitudinal direction. From the fiber mode strain dependent constitutive equations presented in Eq. (31) and (32), it can be seen that the softening behavior is approximated by an exponential function, which is triggered when the equivalent strain is greater than the value of fiber strength over the eigenvalue.

$$\sigma_T^{(3)} = \begin{cases} \varepsilon \cdot \lambda^{(3)} & \text{if } \varepsilon \leq \frac{s^{(3)}}{\lambda^{(3)}} \\ s^{(3)} \cdot \mathrm{Exp}\left[-\left(\frac{\varepsilon - \frac{s^{(3)}}{\lambda^{(3)}}}{k_{bt}^{(3)}}\right)^{3/4}\right] & \text{if } \varepsilon > \frac{s^{(3)}}{\lambda^{(3)}} \end{cases} \tag{31}$$

$$\sigma_C^{(3)} = \begin{cases} \varepsilon \cdot - \lambda^{(3)} & \text{if } \varepsilon \leq \frac{c^{(3)}}{\lambda^{(3)}} \\ c^{(3)} \cdot \mathrm{Exp}\left[-\left(\frac{\varepsilon - \frac{c^{(3)}}{\lambda^{(3)}}}{k_{bc}^{(3)}}\right)^{3/4}\right] & \text{if } \varepsilon > \frac{c^{(3)}}{\lambda^{(3)}} \end{cases} \tag{32}$$

As the calibration process was underway, however, another issue surfaced as seen in Fig. 4.4. From the figure we can clearly see various bumps or spikes are spotted during material softening, at which the stresses increase with increasing strain. This is physically impossible as the load carrying capacity of the material cannot increase in this phase. After some close investigation on the code and the constitutive model, the root of the problem was found to be that the way the strength distribution was set up in the microplane framework, for which promoted groups of microplanes softening occurred in between another groups of microplanes that have not yet reached the softening limit.

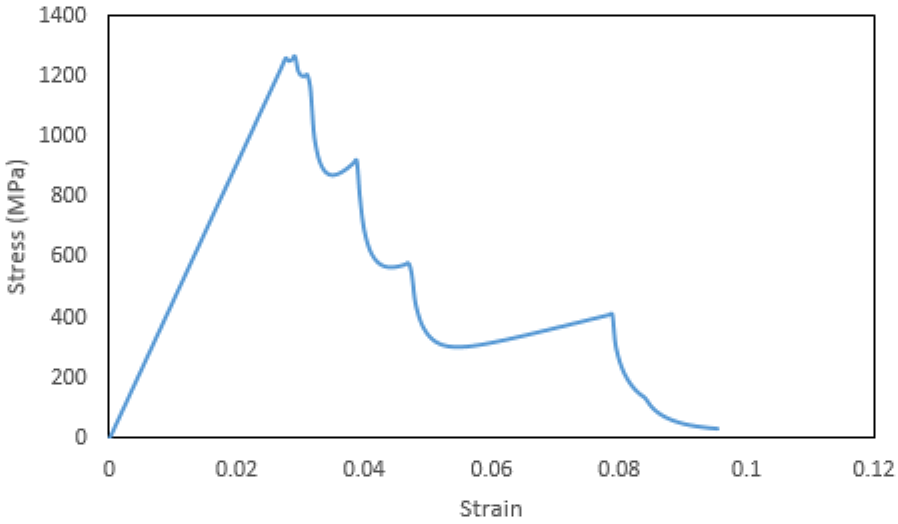

Figure 4.4: Stress-strain curve showing erroneous material behavior in the inelastic regime.

Before running into this roadblock, the strength distribution that indicates the onset of the softening regime for microplane has always been set up as a unit sphere, as illustrated in a two-dimensional sense in Fig. 4.5a. With this configuration, however, as the strain is taking place in the longitudinal direction, indicated by the black arrow, microplanes that are orientated normal to this direction are going to see their normal strain exceeding the elastic limit the soonest whereas the microplanes that are normal to the other two directions (transverse direction) experience softening relatively late. Therefore, the stress-strain curve above in Fig. 4.4 captures this improbable behavior where a group of microplanes softens and continues to dissipate energy all the way until their load carrying capability diminishes followed by another group that are still within elastic regime that results in the spikes in stress. This incorrect behavior repeats a number of times as the entire composite structure dissipates more energy all the way to the final failure.

To address this issue, which is caused by uniform distribution of the strength, an ellipsoidal distribution for the strength is proposed, illustrated in Fig. 4.5b.

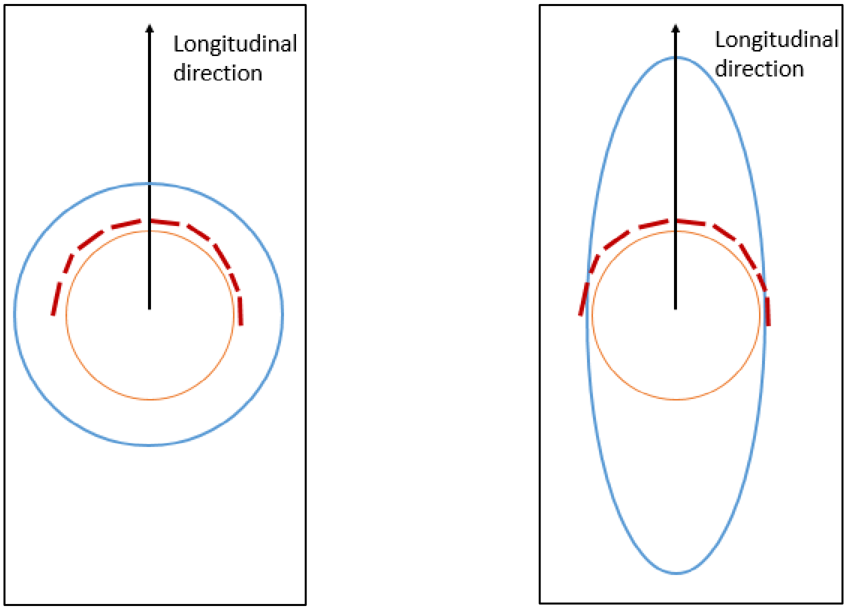

(a) (b)

Figure 4.5: Simplified 2D schematic representation of element (orange), microplane distribution (red), and strength distribution (blue) for (a) a unit circle (b) an ellipsoidal area

The proposed solution is to set up the microplane strength as a function of the microplane orientations like the ellipsoidal shape shown in Fig. 4.6.

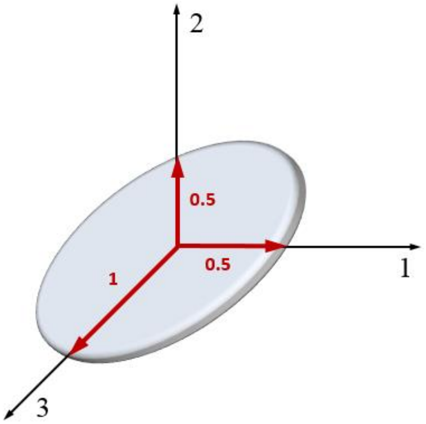

Figure 4.6: Ellipsoidal configuration of the strength distribution in the microscopic scale.

where the coefficient are roughly estimated with unity in the longitudinal direction since it is ideal to have the largest strength value in this direction in order to “delay” the softening. Mathematically, the figure can be interpreted in equation form such that

$$\left(s^{(3)}\right)^2\left(\frac{\sin^2\theta\cos^2\phi}{{s^{(3)}}^2}+\frac{\sin^2\theta\sin^2\phi}{\left(0.5\cdot s^{(3)}\right)^2}+\frac{\cos^2\theta}{\left(0.5\cdot s^{(3)}\right)^2}\right)=1 \tag{33}$$

where $s^{(3)}$ is the microplane strength at which material yielding starts. Then the value of $s^{(3)}$ is solved for as:

$$s^{(3)}=\sqrt{\frac{1}{\left(\frac{\sin^2\theta\cos^2\phi}{{s^{(3)}}^2}+\frac{\sin^2\theta\sin^2\phi}{\left(0.5\cdot s^{(3)}\right)^2}+\frac{\cos^2\theta}{\left(0.5\cdot s^{(3)}\right)^2}\right)}} \tag{34}$$

With the ellipsoidal distribution for microplane strength set up in the constitutive model, the calibration process can be continued as described above and the following values are obtained that demonstrate excellent fit with the experimental data.

Table 4.3: Calibration parameters for longitudinal loading conditions

Description	Symbol (units)	Calibrated value
Mode 3 elastic eigenvalue	$\lambda^{(3)}$ (MPa)	46223
Microplane peak stress in tension	$s^{(3)}$ (MPa)	1440
Microplane peak stress in compression	$c^{(3)}$ (MPa)	900
Parameter governing post-peak softening in tension	$k_{bt}^{(3)}$ (-)	0.01
Parameter governing post-peak softening in compression	$k_{bc}^{(3)}$ (-)	0.01

The resulting stress-strain curves are shown in Fig. 4.7. Similar as before, only one data point, the peak stress value and its corresponding strain, was reported in the literature for both experiments. Likewise, for the calibration procedure, the elastic part of the curve was matched by adjusting the $s^{(3)}$ and $c^{(3)}$for the tension and compression, respectively. The values of $k_{bt}^{(3)}$ and $k_{bc}^{(3)}$ were then manipulated to match the target fracture energy, which is roughly $40\,{}^{N}\!/_{mm}$ and $25\,{}^{N}\!/_{mm}$ for tension and compression, according to [2].

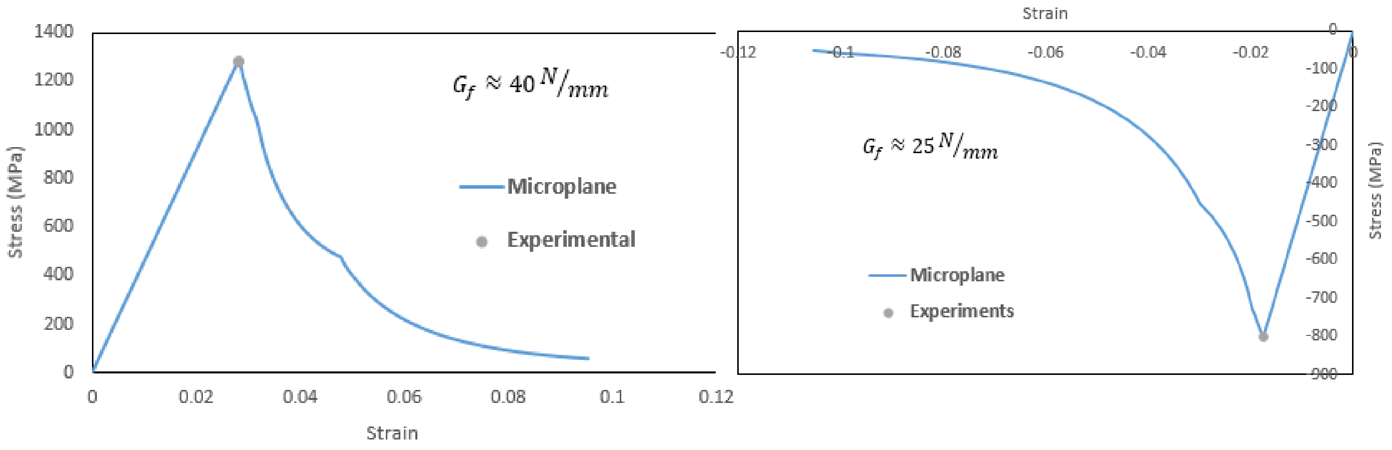

(a) (b)

Figure 4.7: Stress-strain curves of the composite laminate in the presence of uniaxial loading in (a) tension; (b) compression in the longitudinal direction

Chapter 5

Conclusion

The present study proposes a theoretical framework, exploiting the spectral decomposition theorem, a powerful tool to decompose and analyze general anisotropic materials. Through this theorem, the mechanical behavior of laminate composites can be subdivided into characteristic loading conditions representing the longitudinal tension or compression, transverse tension and compression, and shear. The main advantage of the spectral stiffness microplane model is that unlike the composite analysis formulation available today in the market and academia, it can capture the failure envelops and the post-peak material behavior, which include strain softening damage and fracture mechanics aspects. In addition, interactions between multiple spectral decomposed modes have been dealt with for the uni-directional composites. This helps to achieve good fit of the uniaxial data and will help a long way later on if one is decided to carry out multiaxial simulations to examine the failure envelops for the laminate.

5.1 FUTURE WORK

In the present effort, the material calibration was done by comparing against results of uniaxial experiments. It is seen that we are able to achieve very close results in this regard. To get a deeper appreciation of the spectral stiffness model, the biaxial simulations should be performed to achieve a better overall calibrated model that is able to simulate real-life structures. On top of that, notched specimen and open-hole tests should also be performed and results should be compared to experimental data to ensure the work consistency of the model. Last but not least, the model should also encompass all different types of uni-directional materials. By changing the elastic properties and some slight change to the calibration parameters, one should be able to model other material configuration with minimal hassle.

REFERENCES

[1] Salviato M., Ashari S.E., Cusatis G. Spectral stiffness microplane model for damage and fracture of textile composites. *Composites Science and Technology*, 137: 170-184 (2016)

[2] Salviato M., Kedar K. Ashari S.E., Bažant Z.P., Cusatis G. Experimental and numerical investigation of intra-laminar energy dissipation and size effect in two-dimensional textile composites. *Composites Science and Technology*, 135: 67-75 (2016)

[3] Taylor GI. Plastic strain in metals. *J Inst Metals*, 62: 307–324 (1938)

[4] Batdorf S.B., Budiansky B., A Mathematical Theory of Plasticity Based on the Concept of Slip. *Nat. Advisory Committee for Aeronautics, Washington D.C.*, Technical Note No. 1871.

[5] Bažant Z.P., Oh B.H. Microplane model for progressive fracture of concrete and rock. *J Eng* Mech, 111: 559–582. ASCE (1985).

[6] Bažant Z.P., Microplane model for strain-controlled inelastic behavior. In: Desai CS, Gallagher RH, editors. Chapter 3 in mechanics of engineering materials. London: J. Wiley; 45–59 (1984).

[7] Bažant Z.P., Prat P.C. Microplane model for brittle plastic material: I Theory. *J Eng Mech*, 114: 1672–1688 (1988).

[8] Bažant Z.P., Xiang Y, Prat P.C. Microplane model for concrete. I. Stress–strain boundaries and finite strain. *J Eng Mech*, 122: 245–254 (with errata 123:411) (1996).

[9] Bažant Z.P., Caner F.C., Carol I., Adley M.D., Akers S.A. Microplane model M4 for concrete. I: formulation with work-conjugate deviatoric stress. *J Eng Mech*, 126: 944–953. ASCE (2000).

[10] Bažant Z.P., Di Luzio G. Nonlocal microplane model with strain-softening yield limits int. *J Solids Struct*ure,41: 7209–7240 (2004).

[11] Bažant Z.P., Caner F.C. Microplane model M5 with kinematic and static constraints for concrete fracture and anelasticity. I: theory. J Eng Mech 2005;130:31–40.

[12] Caner F.C., Bažant Z.P. Microplane model M6 for fiber reinforced concrete Proc., in: XI Int. Conf. on Computational Plasticity Fundamentals and Applications, COMPLAS, Barcelona, Spain, 796–807 (2011).

[13] Caner F.C., Bažant Z.P. Microplane model M7 for plain concrete. I: formulation. *J Eng Mech*, 139: 1714–1723. ASCE (2013).

[14] Chen X, Bazˇant ZP. Microplane damage model for jointed rock masses. *Int J Numer Anal Met*. 38 (14): 1431–1452 (2014).

[15] Thomson W. Mathematical theory of elasticity encyclopedia britannica, vol. 7, pp. 819–825 (1878).

[16] Elbing K. Foundations of anisotropy for exploration seismics. Oxford: Pergamon Press; 1994.

[17] Soden P.D., Hinton M.J., Kaddour A.S. Lamina properties, lay-up configurations and loading conditions for a range of fibre reinforced composite laminates, Chpater 2.1. *Failure Criteria in Fibre Reinforced Polymer Composites* (2004).

[18] Bažant Z.P., Planas J. Fracture size effect in concrete and other quasibrittle materials. CRC, Boca Raton, FL (1998).